Precise Throughput Determination of the PanSTARRS Telescope and the Gigapixel Imager using a Calibrated Silicon Photodiode and a Tunable Laser: Initial Results

Precise Throughput Determination of the PanSTARRS Telescope and the Gigapixel Imager using a Calibrated Silicon Photodiode and a Tunable Laser: Initial Results

Christopher W. Stubbs, Peter Doherty, Claire Cramer,
Gautham Narayan, Yorke J. Brown

Department of Physics, 17 Oxford Street
Harvard University, Cambridge MA USA

stubbs@physics.harvard.edu

Keith R. Lykke, John T. Woodward

National Institute of Standards and Technology,
100 Bureau Drive, Gaithersburg MD 20899

John L. Tonry

Institute for Astronomy, University of Hawaii, 2680 Woodlawn Drive, Honolulu HI 96822

ABSTRACT

We have used a precision calibrated photodiode as the fundamental metrology reference in order to determine the relative throughput of the PanSTARRS telescope and the Gigapixel imager, from 400 nm to 1050 nm. Our technique uses a tunable laser as a source of illumination on a transmissive flat-field screen. We determine the full-aperture system throughput as a function of wavelength, including (in a single integral measurement) the mirror reflectivity, the transmission functions of the filters and the corrector optics, and the detector quantum efficiency, by comparing the light seen by each pixel in the CCD array to that measured by a precision-calibrated silicon photodiode. This method allows us to determine the *relative* throughput of the entire system as a function of wavelength, for each pixel in the instrument, without observations of celestial standards. We present promising initial results from this characterization of the PanSTARRS system, and we use synthetic photometry to assess the photometric perturbations due to throughput variation across the field of view.

Subject headings: Instrumentation: detectors, photometers; Surveys; Techniques: photometric

1. INTRODUCTION

Multiband ground-based photometry plays a central role in a variety of forefront topics in astrophysics. Examples include mapping the expansion history of the Universe with type Ia supernovae, determining redshifts to galaxies and clusters using photometric redshifts, monitoring the spectral evolution of gamma ray bursts, and detecting and characterizing extrasolar planets with transits.

A specific contemporary scientific objective that requires a clear understanding of system sensitivity across filter bands is using type Ia supernovae to probe the history of cosmic expansion. Imagine that the spectrum of supernova emission were concentrated in a narrow wavelength range, $\delta\lambda$. Observing supernovae at increasing redshift would move the center of emission into redder passbands. In order to precisely compare the luminosity distance vs. redshift, we must clearly have a careful calibration of the *relative* sensitivity across the passbands of interest, with a well-understood metrology foundation. Ascertaining the equation of state parameter $w = P/\rho$ of the dark energy, and searching for any variation with redshift, will require supernova flux measurements with percent or better *precision* (*e.g.* Linder (2009)). The SNLS collaboration has assessed photometric calibration as the dominant source of systematic uncertainty in their program to measure the equation of state parameter w of the dark energy (Regnault *et al.* 2009).

Another opportunity for exploiting high accuracy astronomical flux measurements will arise with the launch of the Gaia astrometric satellite mission, which should provide $\sim 10^5$ stars with distances accurate to better that 0.1% (Perryman *et al.* 2001). Providing a commensurate *accuracy* for photometric measurements will allow for detailed comparisons between observed stellar luminosities and model atmospheres.

These ground-based photometric measurements face a number of calibration challenges. One is knowing the instrumental sensitivity as a function of wavelength. Another is accounting for absorption and scattering in the Earth's atmosphere. The traditional methodology of photometric calibration uses some combination of (1) observations of standard sources at the same airmass as the program objects, or (2) measurements of extinction coefficients in the passbands of interest. In this approach, the spectra of celestial sources constitute (often implicitly) the standard for the measurement. These spectrophotometric standards are either based on ground-based blackbody measurements made decades ago (Hayes & Latham 1975; Megessier 1995), or in the case of DA white dwarfs, on theoretical model atmospheres (*e.g.* Holberg & Bergeron (2006)). Since broadband CCD photometry of celestial sources takes an integral of photon flux across a broad optical passband (u, g, r, i, z or y, for example), it is an ill-posed problem to infer the system sensitivity function vs. wavelength from broadband photometric data alone, especially through a variable atmosphere.

The determination of the effective system throughput has often been done in a piecemeal fashion, taking benchtop measurements of filter transmission, optical catalog values for reflectivity and glass transmissions, and vendor descriptions of typical detector quantum efficiency (QE). The cumulative systematic errors in this procedure limit the precision that can be achieved, and this approach lacks resolution at the pixel scale. Attempting to adjust passbands determined in this fashion to match observations to synthetic photometry is ambiguous: should the passbands be broadened, shifted up or down in wavelength, or should a grey multiplicative scaling be applied?

In order to address these concerns, and to push towards an improvement in photometric precision and accuracy, Stubbs & Tonry (2006) advocated breaking the spectrophotometric calibration problem into two distinct measurements: 1) the determination of instrumental sensitivity, using laboratory-calibrated detectors as the fundamental metrology standard, and 2) measuring directly the optical transmission of the atmosphere. We will focus here on our implementation of a technique for measuring, *in situ*, the relative throughput of the entire PanSTARRS apparatus, relative to a calibrated photodiode.

We can forgo the use of a celestial calibration *source* in favor of a well calibrated *detector* as the fundamental metrology reference for astronomical photometry. National Institute of Standards and Technology (NIST) has calibrated Silicon photodiode quantum efficiencies at the 10^{-3} level. This is an order of magnitude more precise than any celestial spectrophotometric source, either empirical or theoretical. In fact, the primary SI metrology reference for electromagnetic flux is now detector-based rather than source-based (Larason *et al.* 1998). There is ongoing progress at NIST in extending both the wavelength range and accuracy of detector calibration for metrology applications.

We assert that no celestial spectrophotometric source currently offers a photon spectral distribution that is known at the 10^{-3} level, and the prospect of achieving this precision is one of the main attractions of the method described here.

This paper presents promising initial results from an integrated measurement of the total system throughput. We use full-pupil illumination with monochromatic calibration light to measure the entire optical train of the apparatus, including the mirror, corrector optics, filter and detector. The spatial resolution is at the pixel scale, with 1 nm spectral resolution. An earlier realization of this technique, with the Mosaic imager on the 4 meter Blanco telescope at CTIO, was described in Stubbs *et al.* (2007b).

The determination of and correction for variation in atmospheric transmission is a significant challenge. A companion paper (Burke *et al.* 2010) describes progress in the precise determination of atmospheric transmission. We also refer the interested reader to

Stubbs & Tonry (2006) and Stubbs *et al.* (2007a) for a discussion of this issue. The Pierre Auger collaboration has implemented (Auger collaboration 2010) a comprehensive suite of atmospheric monitoring instruments for the calibration of optical transmission in atmospheric fluorescence detection of high energy cosmic rays, and we advocate taking a similar approach for optical and infrared astronomical observations.

The merits of achieving improved photometric accuracy are spelled out in Kent *et al.* (2009), and there is considerable work under way to achieve improved accuracy and precision. Many of these are described in Sterken (2007). The ACCESS project (Kaiser *et al.* 2007) plans to conduct precise spectrophotometry from a sounding rocket. Bohlin (2007) describes spectrophotometric measurements at the 1% level using HST. Adelman and colleagues (Adelman *et al.* 2007) are pursuing ground-based precision spectrophotometry. High *et al.* (2009) describe the use of the stellar locus in color-color space for precise color determinations. Albert *et al.* (2009) discussed the merits of a satellite-based calibration source, which would provide an opportunity to determine both atmospheric transmission and apparatus throughput in the same measurement, providing the satellite could be accurately tracked by the telescope.

The Sloan Digital Sky Survey has used monochromatic light to measure and monitor the spectral sensitivity function of the SDSS camera when removed from the telescope (Doi *et al.* 2010). Our approach uses full aperture illumination of the entire optical system rather than measuring only the camera's response.

We are not currently attempting to establish an absolute calibration of the PanSTARRS system, in units of photons cm^{-2} s^{-1} nm^{-1}, but rather to establish the *relative* system throughput across wavelength, in arbitrary units. A specific example of the importance of understanding the relative photometric zeropoints across filters is when type Ia supernovae are used to map out the history of cosmic expansion. A complete understanding of the effective system passband, and the associated zeropoints, is essential. Type Ia supernova cosmology is one of the many science objectives planned for the PanSTARRS survey. A single measurement of absolute detection efficiency, at one wavelength, would suffice to place the data presented here onto an absolute flux scale. An approach to full-aperture determination of absolute detection efficiency is described by the Auger collaboration in Brack *et al.* (2004).

The calibration technique described here can be used in conjunction with more traditional photometric calibration methods. Using a diversity of calibration methodologies provides an opportunity to assess consistency and to quantify potential sources of systematic error. This approach is not limited to imaging instruments. Spectrophotometric sensitivity functions for dispersive instruments can be acquired in a similar fashion.

A specific motivation for our calibration program is the requirement of knowing the system throughput well enough to perform high confidence color determination for the PanSTARRS survey. As described below, this technique also allows us to monitor filter transmission curves (to check for variation due to hygroscopic effects, for example), and any other changes in instrumental performance.

This paper first presents an overview of the experimental method and apparatus in Section 2, and the observations we obtained in Section 3. Data processing is outlined in Section 4, and results are shown in Section 5. Section 6 presents a preliminary assessment of potential sources of systematic error, followed by our conclusions in Section 7.

2. EXPERIMENTAL METHOD AND APPARATUS

We have implemented the calibration philosophy outlined in Stubbs & Tonry (2006), which exploits the availability of well-calibrated detectors to characterize astronomical apparatus. The reader is strongly encouraged to consult that paper for a full description of the motivation of this approach, and the related formalism.

Our system uses the smooth and well-characterized detection efficiency of a NIST-calibrated photodiode as the standard against which we calibrate the apparatus. The main principle of this technique is to establish the QE(λ) curve of the calibration photodiode as the metrology foundation for the relative throughput measurement. Figure 1 shows the smooth dependence of the photodiode QE vs. wavelength.

An overall conceptual diagram of the arrangement of the apparatus is shown in Figure 2. We project light from a tunable laser onto the flat-field screen in the dome. This screen provides full-aperture illumination of the PanSTARRS telescope. We measure the flux from the screen with a calibrated photodiode. We then compare the flux detected by each pixel in the instrument to that detected by the calibrated photodiode.

Performing this measurement at a succession of discrete wavelengths allows us to determine full system throughput as a function of wavelength. By interspersing calibration images with equivalent exposure times taken with the laser off, we can compensate for flux from ambient light in the dome.

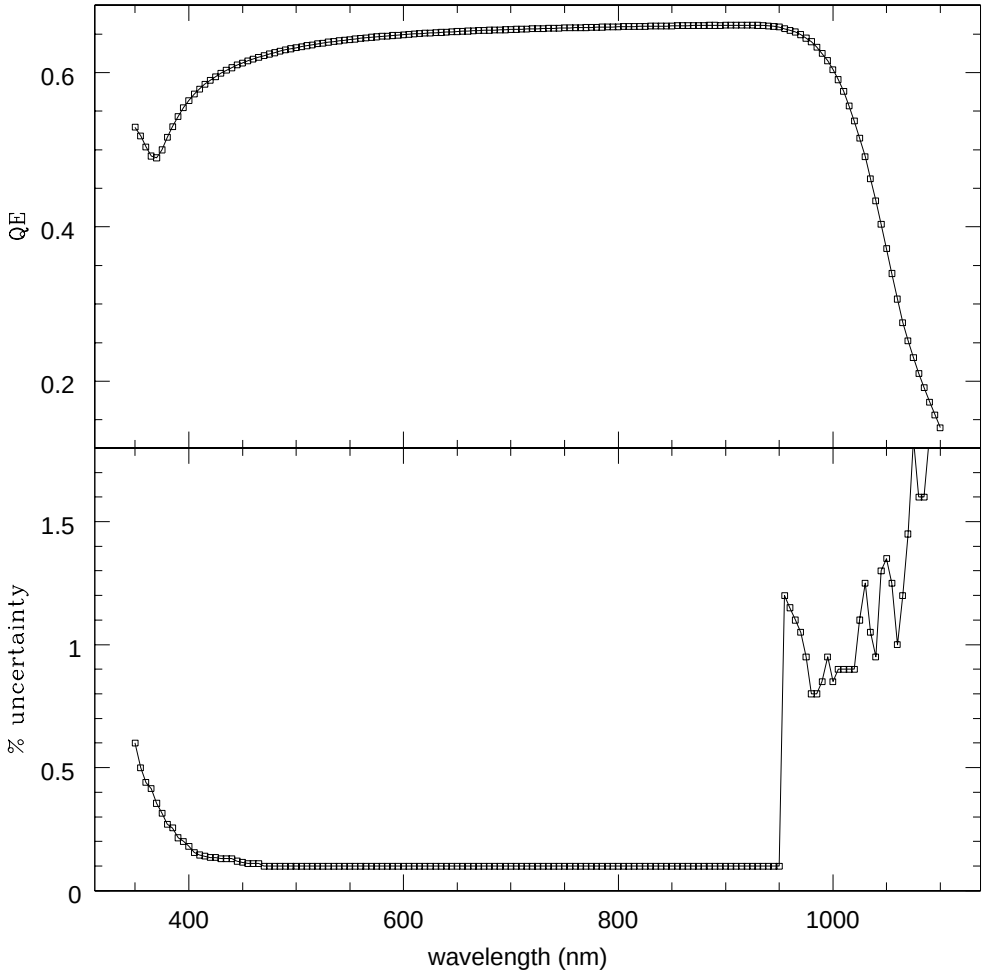

Fig. 1.— Quantum Efficiency Curve and Fractional Uncertainty for NIST-calibrated Photodiode. The upper plot shows the photon detection efficiency vs. wavelength for a Hamamatsu 2281 photodiode. This calibrated response curve is the standard against which we measure system throughput, and is better determined than any celestial spectrophotometric source. The lower panel shows that over the majority of the wavelengths used for CCD imaging, for the photodiode we used the fractional calibration uncertainty in QE is 0.1%. Only in the y band, with $\lambda > 950$ nm, and for $\lambda < 400$ nm (which PanSTARRS does not use) is this photodiode's calibration poorer than a part per thousand. The discontinuous jump in calibration uncertainty for $\lambda >$950 nm arises from a change in the metrology comparison method used by NIST in 2005, when our reference diode was calibrated. More recent work at NIST (Eppeldauer *et al.* 2009) extends high precision calibration out to 1.6 μm, with the prospect of achieving 0.01% accuracy.

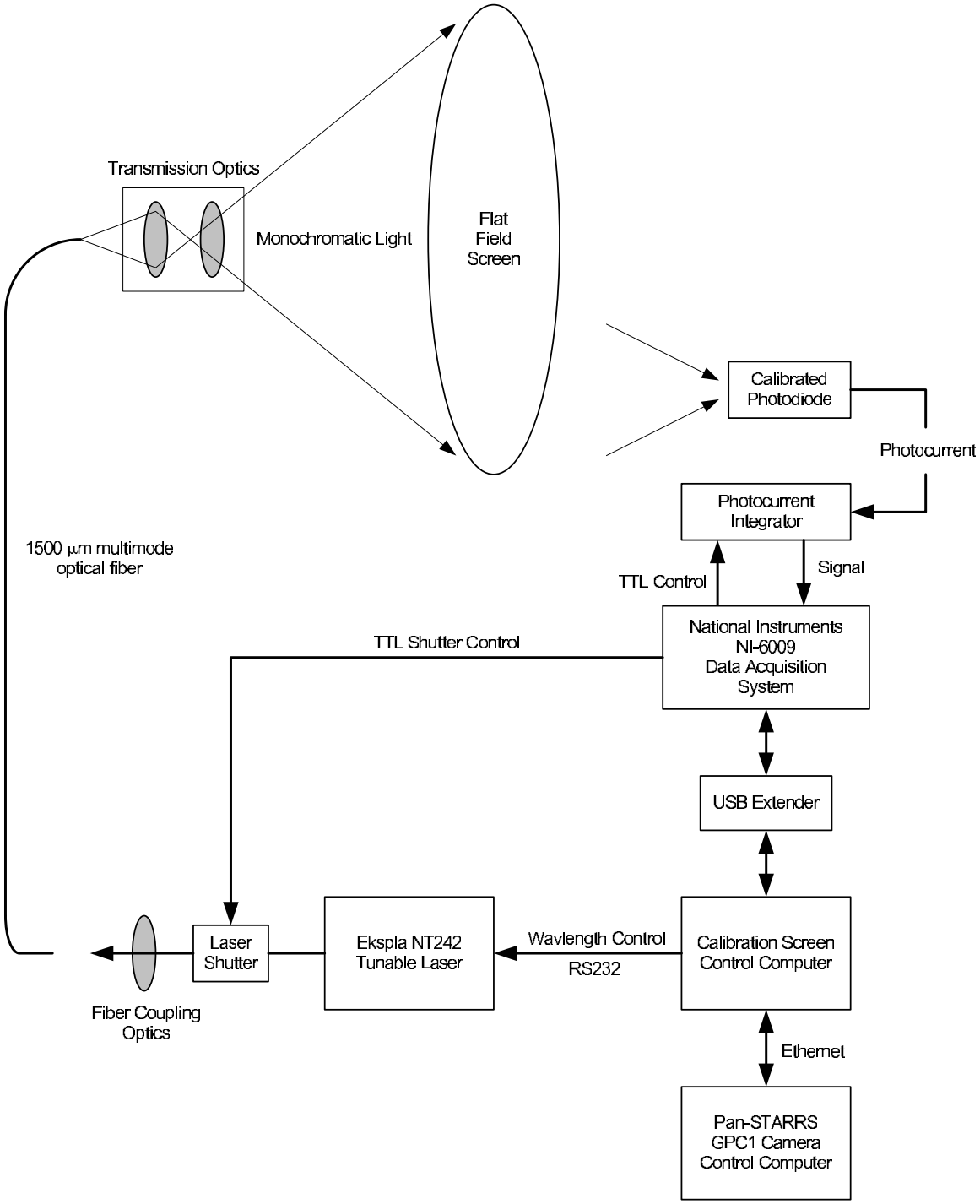

Fig. 2.— Schematic diagram of calibration system configuration. Monochromatic light from the tunable laser is projected onto the full-aperture flat-field screen. The calibrated photodiode is used to monitor the total laser light delivered to the input pupil.

2.1. The PanSTARRS Telescope and the Gigapixel Imager

The PanSTARRS system is a high etendue wide-field imaging system, designed for dedicated survey observations. The system is installed on the peak of Haleakala on the island of Maui in the Hawaiian island chain. Routine observations are conducted remotely, from the Waiakoa Laboratory in Pukalani. We provide below a terse summary of the PanSTARRS survey instrumentation. Further details can be obtained from the project's web site.[1]

2.1.1. The PanSTARRS Survey Telescope

The PanSTARRS optical train uses a 1.8 meter diameter $f/4.4$ primary mirror, and a 0.9 m secondary. The resulting converging beam then passes through two refractive correctors, a 48 cm $\times$ 48 cm interference filter, and a final refractive corrector that is the dewar window.

2.1.2. The PanSTARRS Gigapixel Camera

The PanSTARRS imager (Tonry *et al.* 2008) comprises a total of 60 4800 $\times$ 4800 pixel detectors, with 10 μm pixels that subtend 0.258 arcsec. The total field of view of the system is 3.3 degrees. The detectors are back-illuminated CCDs manufactured by Lincoln Laboratory. The detectors are read out using a StarGrasp CCD controller (Onaka *et al.* 2008), with a readout time of 7 seconds for a full unbinned image.

The CCDs in the PanSTARRS camera are deep-depletion devices, 75 μm thick, which increases the QE in the region around 1 μm and minimizes the effect of fringing from sky lines. The instrument has a filter changing mechanism that contains 6 large-format interference filters, g,r,i,z,y and w.

The temperature of the CCD array was -75C, for the data presented here. For the y band, where the red edge of the passband is partially defined by the falling silicon QE curve, the detector QE is temperature sensitive. We made explicit note of the temperature registered by the StarGrasp controller for each flat-field image obtained. In the future we expect to measure the temperature dependence of the system efficiency, arising in the detectors because of this phonon-assisted photoconversion regime in silicon.

[1] `http://pan-starrs.ifa.hawaii.edu/public/project-status/project-status.html`

The shutter for the Gigapixel array is a dual-blade linear curtain shutter, that provides millisecond-accuracy timing information on actual shutter open times. This accuracy and repeatability is important for proper background subtraction if ambient light correction is substantial. Our method ensures that the shutter is fully open during the interval over which we inject laser light, so even instruments with iris-type shutters could be calibrated with minimal shutter artifacts.

2.2. Monochromatic Calibration Apparatus

Light from the tunable laser was transported through an optical fiber to a back-illuminated flat-field screen. A photodiode with a transimpedance amplifier was used as a coarse light level monitor, and was useful for adjusting the light intensity to the desired level. The calibrated photodiode monitored the light emanating from a portion of the screen, and was fed into an integrator circuit as described in more detail below. A shutter was used to interrupt the light into the source fiber.

An observing sequence entailed the following stages:

1. Set desired wavelength,
2. Open camera shutter,
3. Wait 1 sec,
4. Open laser shutter,
5. When time or flux threshold satisfied, close laser shutter,
6. Wait 1 sec to ensure full light dose received by camera, and to obtain post-laser ambient light level in photodiode signal,
7. Close camera shutter and read out image
8. Obtain another image and photodiode series, for same camera shutter open time, with laser off, for ambient light compensation.

The tunable laser was located on level 1 of the PanSTARRS dome. A multimode optical fiber, NA=0.3, with low OH content, with a diameter of 1.5 mm, and clad in semirigid conduit

(Ceramoptic part number SMA2/WF1500/1590T30/SS/20.0M) [2] carried the laser light up through the telescope structure and onto an optical bench assembly that was mounted above the flat field screen.

One challenge posed by the PanSTARRS system is that the space available in the dome is minimal. To achieve a full-pupil illumination of the telescope, we constructed a projector box that is mounted on the inner wall of the enclosure. This illuminates a transmissive flat-field screen (obtained from the Day-lite Corporation) that sends calibration light into the front of the telescope. We illuminated the rear of the flat-field screen by sending light that emerged from the fiber through the optical layout shown in Figure 3.

The PanSTARRS enclosure and telescope cannot perform independent rotations in azimuth. The telescope is always in the plane of the enclosure slit. The calibration screen and projector box are therefore mounted "behind" the enclosure slit, and the elevation axis of the telescope is rotated past vertical, to 125 degrees from the horizon, to point at the screen.

Each unvignetted element of area dA on the flatfield screen illuminates every pixel of the imager, since the optical system maps angles at the pupil to position in the focal plane. Each pixel of the imager correspondingly receives light that emanates from the everywhere on the screen, at the angle of arrival that maps onto that pixel. Different regions of the focal plane receive flux from slightly different areas of the illumination screen, but as long as the screen surface brightness distribution is independent of wavelength we can reliably measure the relative spectral response of each pixel.

As long as the illumination pattern on the screen is independent of wavelength, at the 10% level, the laser illumination allows us to determine (at the 1% level or better) the wavelength dependence of the sensitivity of *each* pixel. We can correct for the nonuniform illumination in our laser dome flats in the same way illumination corrections are traditionally used to correct dome flats.

We have also installed a digital micromirror array in the projection box, that can be fed with an optical fiber, and we intend to use this to quantitatively assess the effect of screen illumination non-uniformities. Operating the calibration system in this fashion is the equivalent of projecting an image using a digital projector, except the light source can be either a white light source, or monochromatic light from the tunable laser. This capability was not employed for the results presented here, and so the entries in the systematic error

[2] Certain trade names and company products are mentioned in the text or identified in an illustration in order to adequately specify the experimental procedure and equipment used. In no case does such identification imply recommendation or endorsement by the National Institute of Standards and Technology, nor does it imply that the products are necessarily the best available for the purpose.

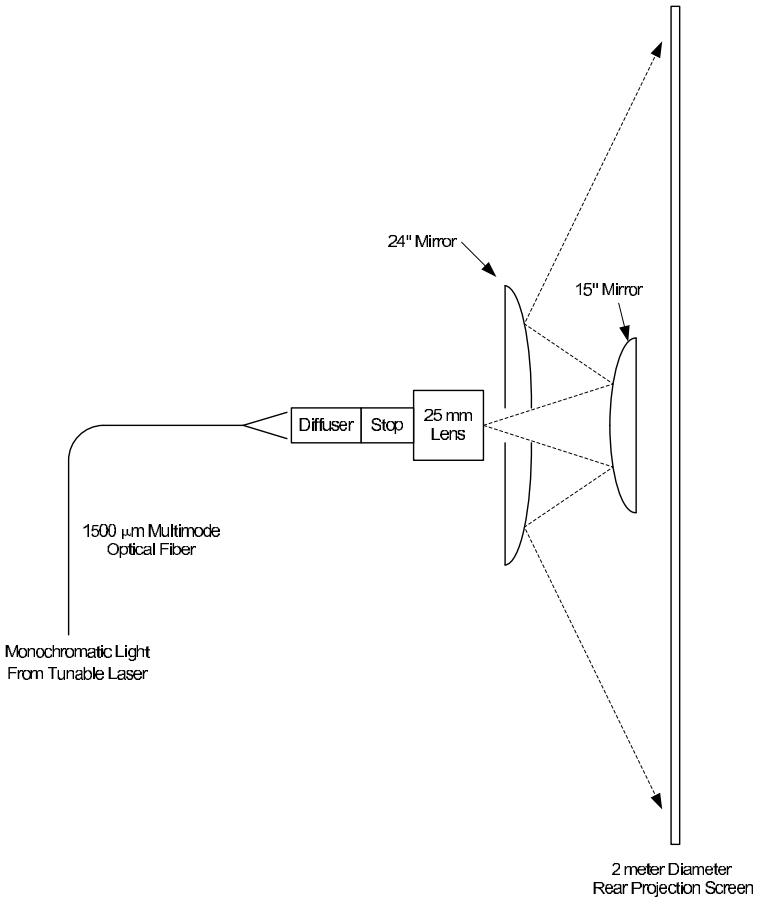

Fig. 3.— Calibration light from the optical fiber is collimated with an achromatic 25mm focal length lens, followed by an engineered diffuser. An aperture stop after the diffuser is imaged onto a backlit flatfield screen using a combination of a broadband lens and a pair of convex acrylic mirrors. The projection system produces an image of the aperture on the back-illuminated transmissive flatfield screen. The calibration diode monitors light that emanates from the screen.

budget due to illumination non-uniformity contain estimates, for the time being.

2.3. Tunable Laser Source.

We used an Ekspla NT242 OPO laser as a tunable source of monochromatic light. A 1 KHz pulsed Nd:YAG laser at 1.064 μm is the initial source of photons. This light passes through a pair of non-linear optical crystals that upconvert the light to λ=355 nm. These UV photons are then run through an optical parametric oscillator (OPO) that splits each UV photon into a pair of photons, conserving both energy and momentum. The orientation of the OPO crystal relative to the incident beam can be adjusted so as to select a specific wavelength of interest. The wavelength of the output beam can thereby be tuned over a wavelength range of 210 nm to 2.3 μm.

From the photon pair produced, the upper or lower frequency light is selected by exploiting the fact that these two beams have orthogonal linear polarizations. There is a "degeneracy point" in the OPO system at $\lambda = 2 \times 355$ nm =710 nm where the OPO power drops, but this did not pose a significant problem. For wavelengths $\lambda < 410$ nm the Ekspla laser uses up-converted light from OPO emission at 2λ, and both the output power and spectral purity are considerably less favorable. We elected in this run not to extend our measurements below 410 nm, pending the installation of a short-pass filter in the beam. Although the light emitted from the Ekspla NT242 OPO is polarized, as the light is transmitted through the optical fiber its polarization becomes randomized.

The 5 nsec Ekspla NT242 OPO pulses have the advantage that the coherence length of the laser light is correspondingly short, so the light on the flatfield screen shows no evidence of speckle patterns that would afflict a continuous narrowband source. The spectral breadth of the tunable light is about 0.1 nm at 400 nm and 0.5 nm at 1 μm. The light intensity from the Ekspla NT242 OPO is somewhat adjustable. The Nd:YAG laser has a variable time delay between the flashlamp pulse and the Q-switch driven dump of the laser cavity. Changing this time delay varies the intensity of the light emitted by the Nd:YAG laser, and hence the intensity of the tuned light as well.

2.3.1. Wavelength Calibration

We used a spectrograph from Ocean Optics (model Jaz) to monitor the wavelength of the light being sent to the flat-field screen. We used this spectrograph in conjunction with a Hg-Ar line lamp module (Ocean Optics HG-1) which constitutes our primary wave-

length standard. We tuned the Ekspla NT242 OPO to a succession of wavelengths that corresponded to lines emitted by the arc lamp source, and we compared the line centroids for the laser light to those from the arc lamps. The results are shown in Table 2.3.1. The table shows the line used, the Ekspla NT242 OPO setting, the reported centroids for the laser and arc lamp, and the magnitude of the centroid difference. The Ekspla NT242 OPO wavelengths are accurate to $\sigma_\lambda \sim 0.2$ nm, comparable to the intrinsic line width of the laser. The wavelength calibration of the laser is more accurate than the wavelength solution of the spectrograph, but we stress that the spectrograph was used only as a *differential* instrument, comparing the wavelengths of the arc lamp to that emitted by the laser.

Table 1: Wavelength Calibration.

Line (nm)	Laser setting (nm)	Laser centroid (nm)	Arc centroid (nm)	|Difference| (nm)
Hg 435.83	435.8	436.8	437.0	0.2
Hg 546.07	546.1	547.7	547.6	0.1
Ar 696.54	696.5	698.1	698.0	0.1
Ar 763.51	763.5	765.3	764.9	0.4
Ar 800.62	800.6	802.2	802.4	0.2
Ar 912.30	912.3	913.1	913.5	0.4

2.4. Monitoring Light with Calibrated Photodiode

We configured a NIST-calibrated silicon photodiode to monitor light emanating from the flat-field screen. The photodiode is a Hamamatsu S2218 whose quantum efficiency was tied to our NIST-calibrated identical part, serial number I220. The calibration diode was equipped with a blackened "snout" tube that limited its angular field of view. The snout tube had a length of 76.2 mm and an inner diameter of 25.4 mm. This limited the photodiode's field of regard to 18 degrees, which from the diode's location spanned about a quarter of the surface of the emissive screen. The temperature of the calibration photodiode for the data presented here was typically around 12^{o}C. By avoiding any imaging optics we avoid introducing any unwanted wavelength dependence in the calibration photodiodes's signal chain.

2.5. Photodiode Electronics and Instrument Interface

The photodiode fed an integrator circuit that we used to monitor the light emitted by the screen. We used a polypropylene 1000 pF capacitor (Panasonic type ECQP) in the integrator. We consider this preferable to a transimpedance amplifier, for a number of reasons. First, the 5 ns pulses from the Ekspla NT242 OPO produce photocurrent bursts from the photodiode, and the finite gain-bandwidth product of a transimpedance configuration essentially attenuates the signal. On the other hand the integrator configuration assures that all the photoelectrons generated in the calibration photodiode eventually appear across the integrating capacitor, with no loss of signal. Perhaps more importantly, we are primarily interested in the total laser light delivered to the system, and this favors the integrator circuit configuration. The integrator output signal then ran through a unity gain buffer amplifier and into the data acquisition system. This light-integration approach was also important in minimizing any deleterious effects due to pulse-to-pulse intensity variations in the Ekspla NT242 OPO output. The integrator was reset on command (with a mechanical relay, to avoid charge injection issues) using one of the digital outputs on the data acquisition module.

The data acquisition module was model NI USB-6009 from National Instruments, with 14 bit A/D conversion and 12 digital input/output bits which was connected to the data acquisition computer with a USB interface.

We did consider potential systematic errors arising from the 5 nsec intense bursts of photons we delivered to the focal plane. The photoconversion response of silicon in this regime has been shown to be linear and well behaved (Stuik & Bijkerk (2002), Vest & Grantham (2003)). This applies to both the CCDs in the instrument as well as the calibration photodiode.

2.6. Data Collection Software and Architecture

We adhered to the overall philosophy of the PanSTARRS system, by establishing the calibration computer as a server that was accessible over the network in the dome. Programs requesting services (such as setting a laser wavelength, etc.) communicated via socket connections to this server. The calibration server computer is a node that is responsible for interfacing with the tunable laser, with the photodiode data acquisition system, and the wavelength monitoring spectrograph.

PanSTARRS collects multi-extenstion FITS images, and appropriate header keywords were populated with sufficient calibration metadata so that the images and their headers

constitute a complete data set for downstream analysis. These header keywords include light dose information from the photodiode and integrator, and the wavelength of the calibration source for each image.

Data collection is scriptable, allowing sequences of wavelengths to be collected automatically. The calibration server allows for two modes of operation. In one, the laser shutter is opened for a fixed period of time. We prefer to use a second mode, where the laser light was kept on until the integrator signal reached a pre-determined threshold. The data presented here were all obtained in the fixed-threshold mode. If the monitor photodiode's quantum efficiency were wavelength independent, this would amount to a fixed dose of photons for each exposure.

3. OBSERVATIONS

We obtained the data presented here on UT Dec 12 and 13, 2009. The majority, but not all, of the observations were obtained at night to minimize deleterious effects of stray light in the dome. We determined that a spacing of 2 nm was adequate to sample the structure in the wavelength-dependent system response, including both filter response function variations and fringing in the CCDs. We obtained a succession of laser-on and laser-off images, each with a corresponding data set from the monitor photodiode. Scanning each filter took about an hour of automated data collection.

3.1. Representative Photodiode Data

Figure 4 shows a typical measurement of the integrated light intensity seen by the photodiode and integrator circuit. The plot shows (at an acquisition rate of 100 samples/sec) the ambient and laser light contributions.

The integrator signal shown in Figure 4 indicates that the ambient light level was well below the laser light level. The integrator time series was analyzed to extract four voltages, corresponding to the start and end points, as well as the transition points where the laser shutter was opened and closed. For the analysis presented here we used only the start and end values V_1 and V_2, as described below.

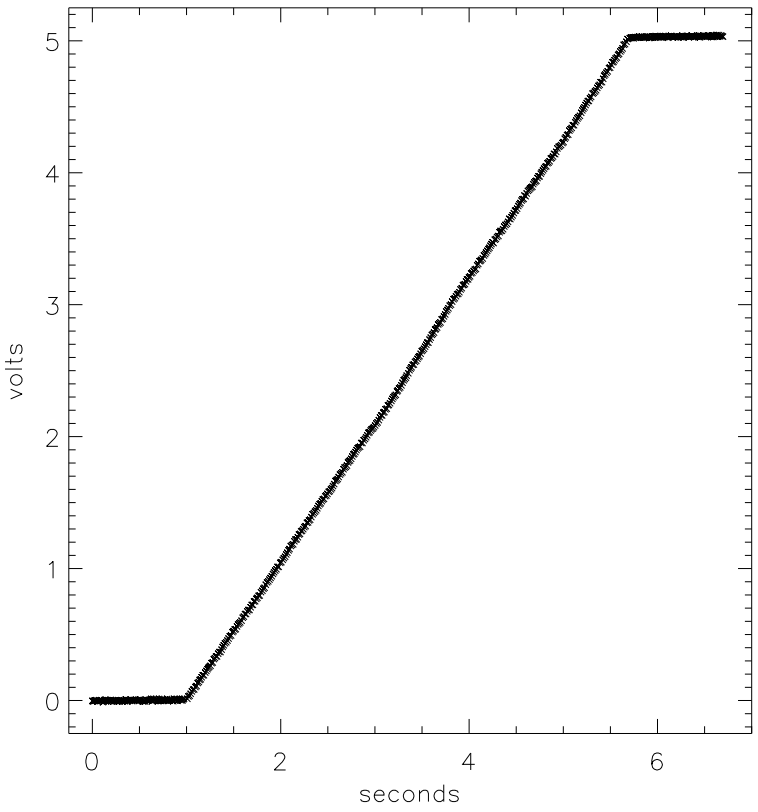

Fig. 4.— Typical integrated calibration diode photocurrent vs. time. The vertical axis is the integrator output (in Volts) which is proportional to integrated photoelectrons. The horizontal axis is time in seconds. The period of laser activity is the steep portion after $t = 1s$. We define the two endpoints as V_1^{on} and V_2^{on} for data taken when the laser is active, and as V_1^{off}, and V_2^{off} in the case when the laser is off. The laser light totally dominates over ambient light levels in the dome, in the example shown here. Furthermore, the slope of the integrated signal is quite constant over the period when the laser is on, indicating good pulse-to-pulse intensity stability for the laser light. The laser shutter was closed when the integrator voltage reached the threshold of 5.0 V.

4. DATA PROCESSING

4.1. Calibration Light Intensity Signal Processing

We digitized and stored the integrated photocurrent signal before, during and after the laser shutter was opened. We determined the start and end integrator voltages, V_1^{on}, V_2^{on}, V_1^{off}, and V_2^{off} respectively, for the laser-on and laser-off images. The difference $\Delta V = V_2 - V_1$ is proportional to the total amount of photocurrent produced by the photodiode while the camera shutter was open. Dividing this value by the photodiode's quantum efficiency provides us with a quantity that is proportional to the number of photons delivered to the input pupil.

4.2. Determination of System Throughput

For each wavelength we computed the fraction of incident photons that each pixel detected. We subtracted an appropriate laser-off frame from each calibration image. This compensates for ambient light in the dome, for any dark current (which in our case is negligible) and for any bias structure in the array. The resulting $\Phi_{laser}(\lambda) = \Phi^{on}(\lambda) - \Phi^{off}(\lambda)$ image was normalized to the number of incident calibration photons, to arrive at a relative system throughput (in arbitrary units that are proportional to ADU's per pixel per incident photon, for pixel i, j) of

$$T(i, j, \lambda) = \Phi_{laser}(i, j, \lambda) QE(\lambda) / (\Delta V^{on} - \Delta V^{off}),$$

where $QE(\lambda)$ is the calibration photodiode's quantum efficiency. The $T(i, j, \lambda)$ data cubes for each filter comprise the system sensitivity data we seek. We stress that this produces a set of efficiency curves for each filter that have a common basis, namely the known detection efficiency of the calibration photodiode.

4.3. Spatial Averaging

We have obtained calibrated throughput data for 1.4 billion pixels at over 350 wavelengths. In order to reduce this data cube to tractable subsets suitable for visualization and human digestion, we have chosen to produce averages over 7 annular regions of the $T(i, j, \lambda)$ frames, with equal dr values.

5. RESULTS

The data collected here can be used in a variety of ways. For this presentation of initial calibration results, we chose to investigate:

1. Short term repeatability of the measurements.
2. A determination of relative system throughput vs. wavelength, tied to a common standard: the response curve of the calibrated photodiode.
3. The absolute transmission function of each filter, by comparing the response function with and without a filter in the beam.
4. Spatial variation in transmission vs. wavelength, radially across the focal plane.
5. A determination of fringing amplitudes vs. wavelength, for the deep depletion CCDs in the PanSTARRS camera.

These are treated in turn, in the subsections that follow.

5.1. Short Term Repeatability

For a few wavelengths in the r band we made a succession of five measurements, spread over the 48 hour period of data acquisition. The means and standard deviations of these repeated data points are presented in Table 2. These figures are for a single annular region on the focal plane. It appears that short term stability is at the level of one to two parts per thousand.

Table 2: Short term Repeatability for 5 Measurements Taken Over 48 hours.

λ (nm)	Mean T (relative to peak)	σ_T
550	0.60	0.0016
554	0.81	0.0018
558	0.88	0.0018
562	0.90	0.0017
566	0.91	0.0063
570	0.90	0.0013
574	0.89	0.0012
578	0.92	0.0012
582	0.94	0.0019
586	0.93	0.0013
590	0.94	0.0016
594	0.94	0.0022
598	0.96	0.0015

5.2. Relative System Throughput Across the PanSTARRS Passbands

We have mapped out the integrated system response for the PanSTARRS optics and camera, with a metrology scheme that allows us to compare the throughput across all passbands. In Figure 5 we show the system throughput curves we measured.

Taken in conjunction with an estimate of atmospheric transmission we can use these curves to compare the *colors* from synthetic photometry of spectrophotometric standards to the colors obtained from the PanSTARRS system.

5.3. Filter Transmission Functions

By dividing the transmission curve obtained with a filter in the beam to that obtained with no filter, we can determine the absolute filter transmission curves with the same angular distribution as light from celestial sources. The filter transmission functions we obtained are shown in Figure 6, for one annular region in the focal plane

Figure 7 compares the benchtop trace of the r band interference filter (Barr Associates 2006) to what we obtained. The microstructure in the main passband is reproduced, and the skirts of the filters show good correspondence. The family of curves we obtained from different annuli in the focal plane shows the same structure in transmission vs. wavelength.

5.4. Spatial Variation in Spectral Response

We explored the variation in response across the focal plane. This is most pronounced at the edges of the filters. Figure 8 shows the field dependence of the r band response of the system. (We see similar radial variations in system response at the filter edges in other passbands as well.) By taking annular averages in system response to produce Figures 7 and 8, we are averaging over any first order gradient in screen uniformity, as discussed in the description of potential sources of systematic error, below.

There is clear evidence for non-trivial response variations between the center and the edge of the field, in the r band. The outer regions of the field have an r-band response that cuts on at a bluer wavelength, and extends to longer wavelengths before cutting off. In addition, there is an overall enhancement in response at longer wavelengths, at the edge of the field . The outer annulus of the instrument appears to have an r band that is a few nm wider, and a response to wavelengths λ >600 nm that is a few percent higher, than the response measured at the center of the field.

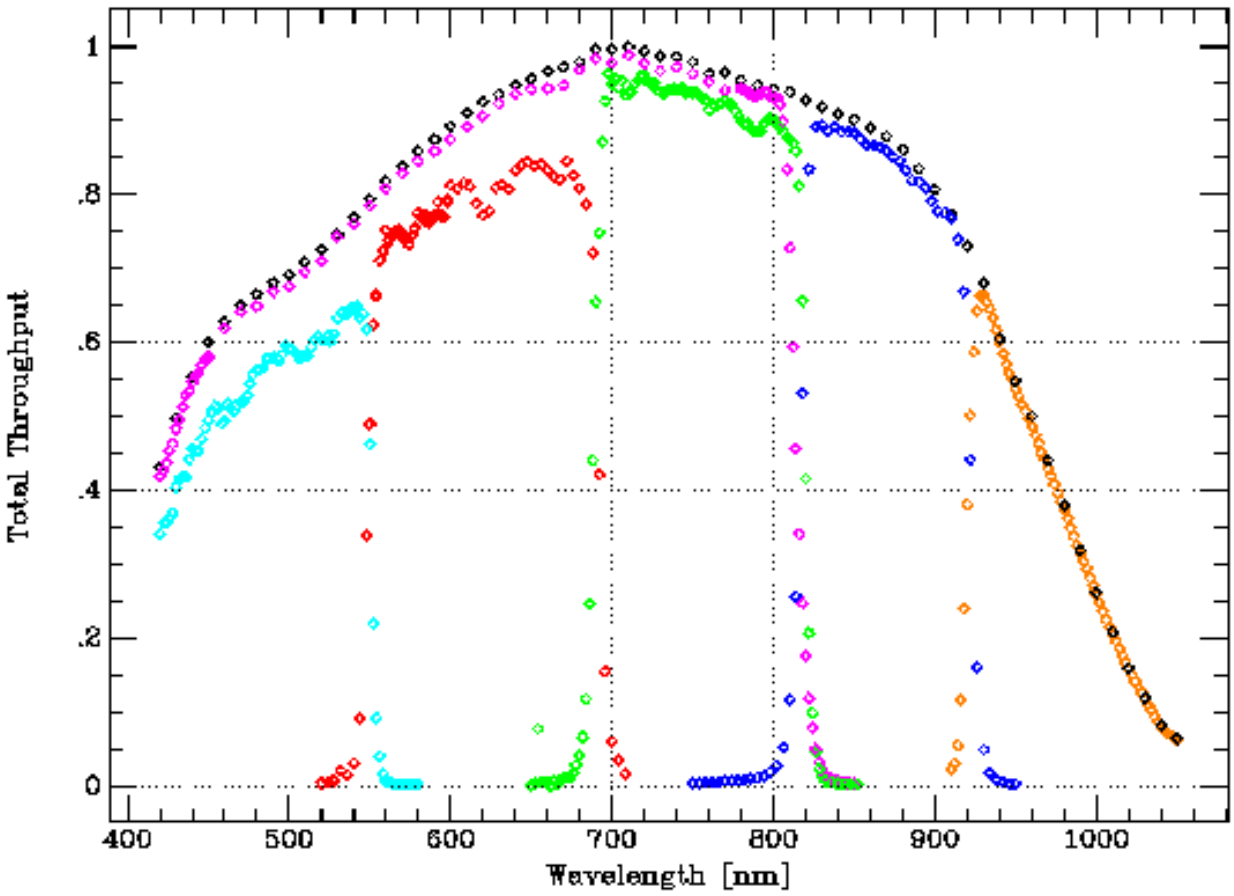

Fig. 5.— PanSTARRS transmission functions, for g (cyan), r (red), i (green), z (blue), y (orange), w (purple) and open (black), determined from full-pupil illumination with tunable laser light. The region between 550 and 600 nm was scanned five times, and shows short term repeatability at the level of a few parts per thousand. Since there is a single overall multiplicative free parameter, we have chosen for this plot to normalize all the curves to the peak sensitivity seen, with no filter in the beam.

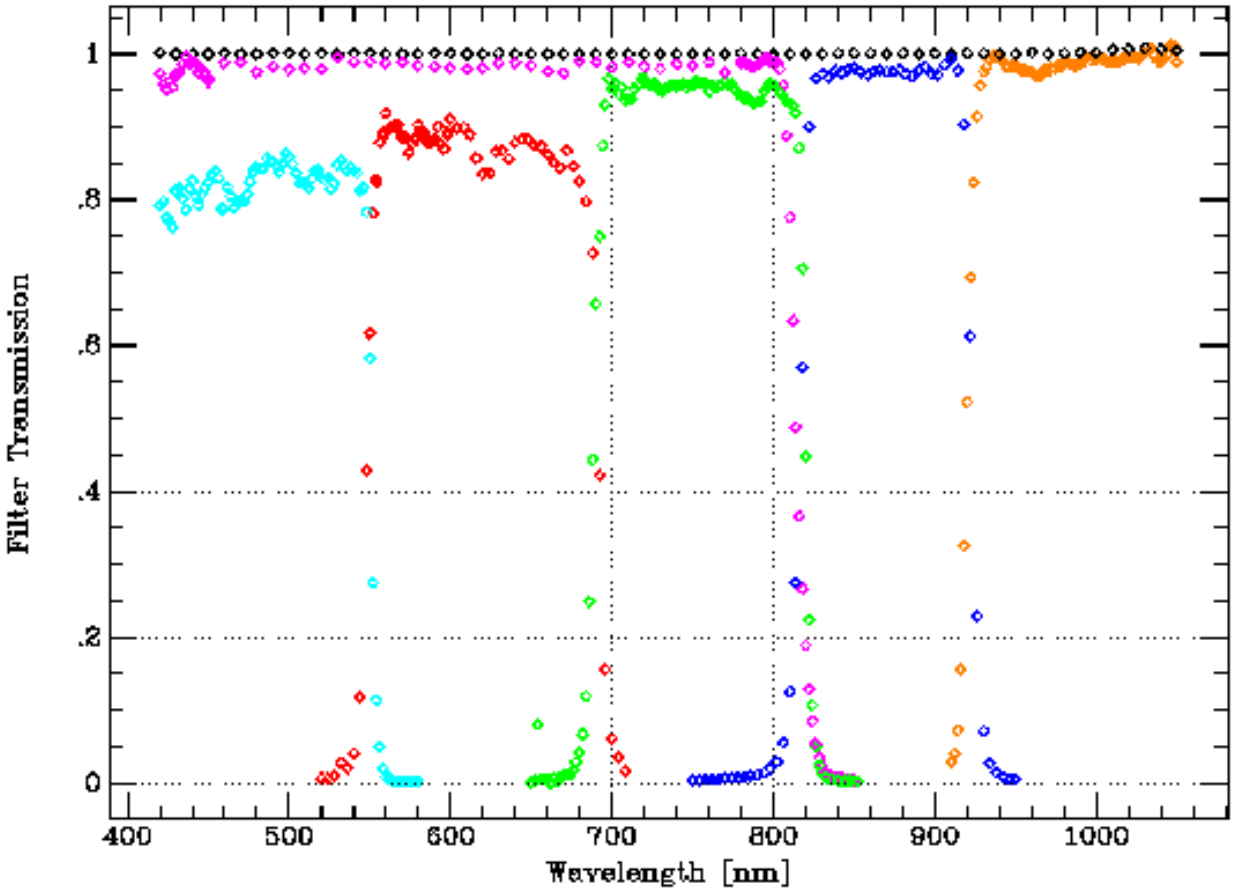

Fig. 6.— PanSTARRS filter-only functions, for g (cyan), r (red), i (green), z (blue), y (orange), w (purple) and open (black). For this plot the vertical axis does correspond to the absolute filter transmission, since these data are the ratio between the measured sensitivity functions with and without the respective filters in the beam.

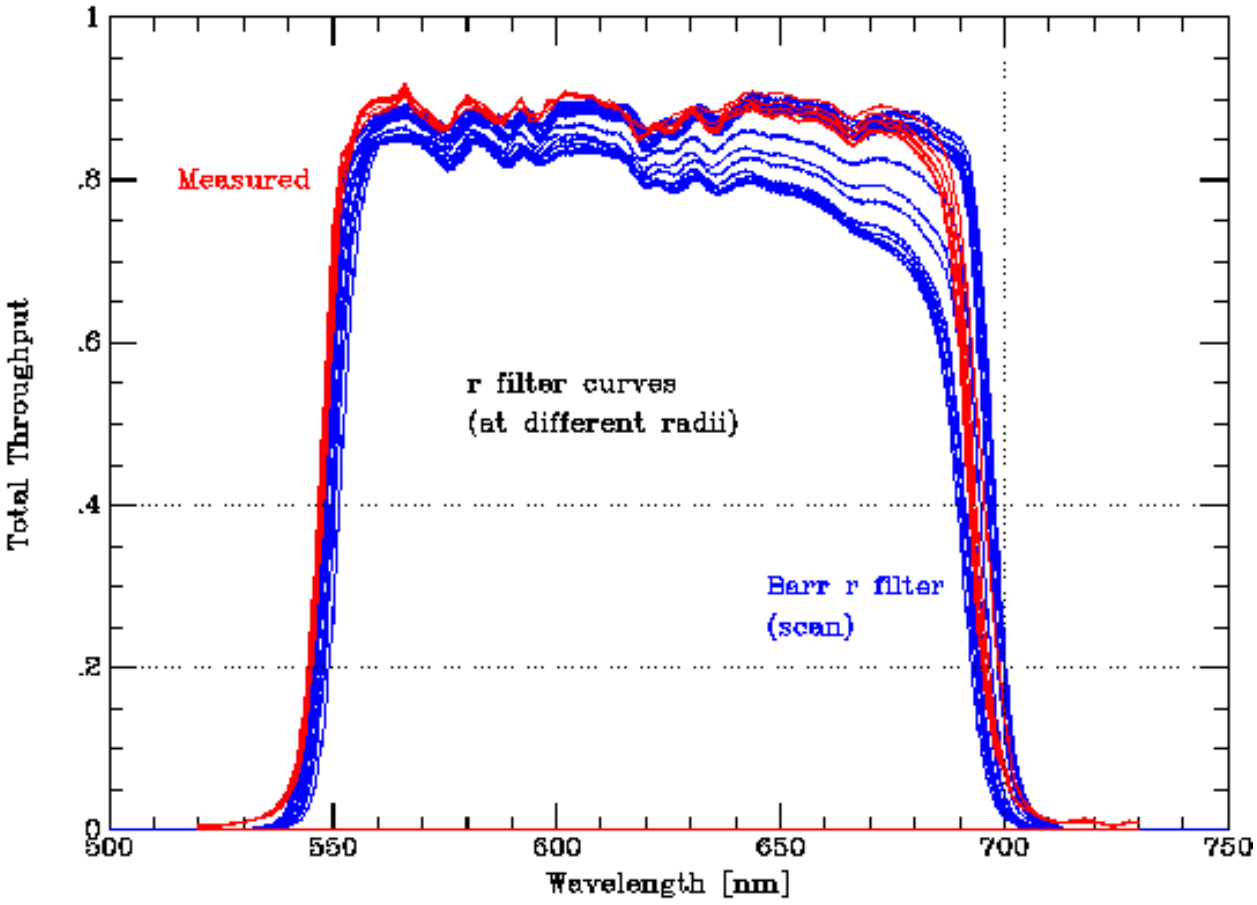

Fig. 7.— This plot compares the radial variation at the focal plane we observed (red) in the Pan-STARRS r filter with the spatial variation in filter transmission reported by the vendor, in collimated light (blue). The vendor curves rise on the red end from 1 to 9 inch radius, and the highest cluster of eight curves are at radius 9.5 inch, on the eight octagonal faces. The microstructure we measure corresponds in detail to that reported by the vendor. The radial dependence at the focal plane (what we measure) is expected to be the convolution of the beam footprint at the filter with the filter's spatial variation in transmission (what the vendor measured), with some perturbation due to the angular distribution of converging rays. The data obtained on the telescope exhibit the shift towards the blue that is characteristic of interference filters for light at other than normal incidence. These complications add motivation to making an integral, full-aperture determination of system throughput, as described in this paper.

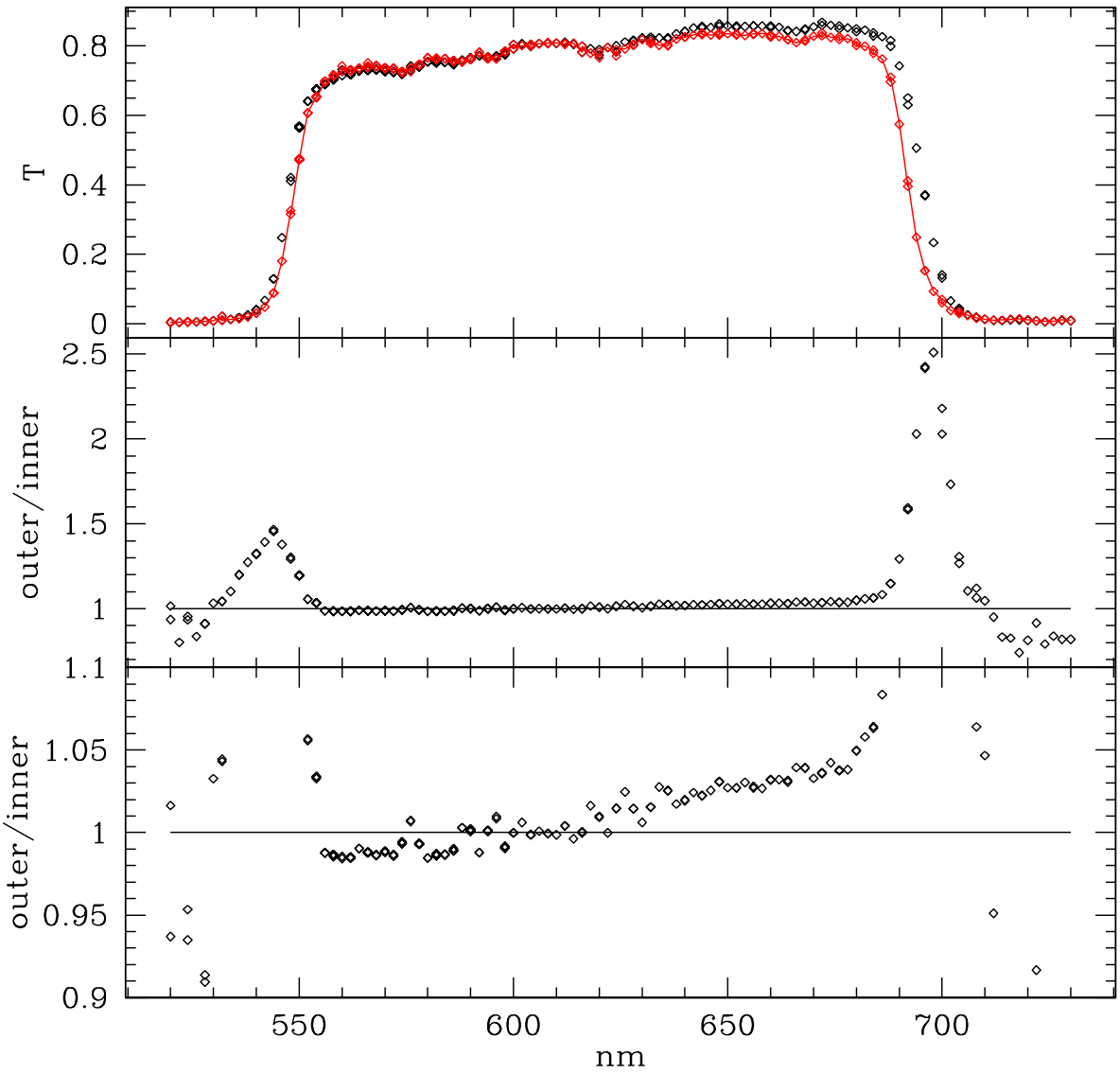

Fig. 8.— The upper panel shows the variation in system response in the r band between the center (red line) and the outer annulus (black points) of the PanSTARRS focal plane. The middle panel shows the ratio $R = outer/inner$ of the system response function, and the lowest panel shows this same ratio at a different scale. There is a shift in the effective passband between the center and the edge of the field, with the outer edge having both an enhanced red response and a wider passband.

A certain amount of this field dependence in the effective passband will be compensated in the process of constructing an illumination correction, *i.e.* by insisting that the natural system magnitudes of sources are independent of position on the focal plane. However the data we show here indicate that we should expect a color-dependent residual.

5.5. Fringing

The deep depletion detectors used in the PanSTARRS camera have significant quantum efficiency in the near infrared (as seen in the "open" curve in Figure 5). This suppresses fringing compared to currently conventional CCDs. Figure 9 shows a full frame obtained in the z band at λ=902 nm.

In conjunction with a spectroscopic measurement of the relative intensity of OH night sky lines, the images we have obtained could in principle be used to construct a spectrally-matched fringe frame for each image taken in the PanSTARRS survey. Even better would be to obtain monochromatic dome flats at the specific wavelengths that correspond to the brightest sky lines, and then make an flux-weighted sum of those images to construct a fringe frame appropriate for each PanSTARRS survey image.

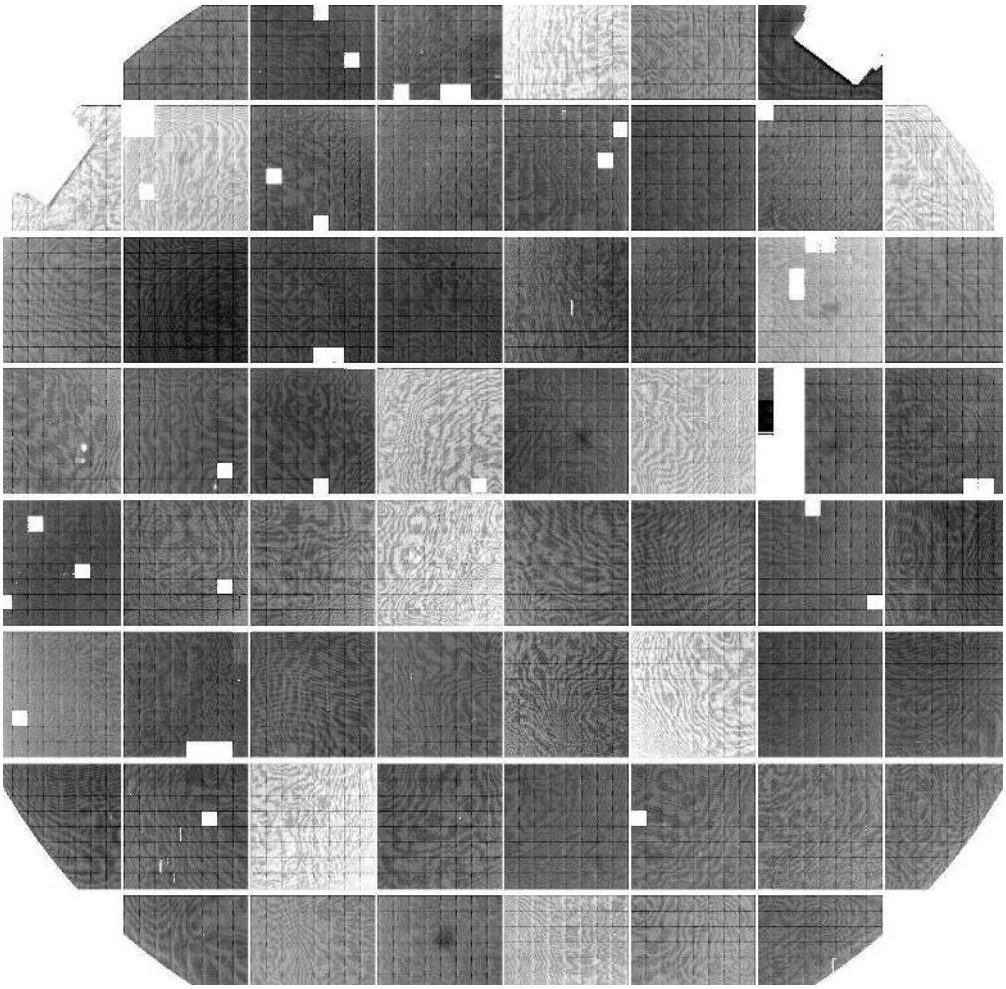

Fig. 9.— Fringing pattern in monochromatic light at 902 nm, in the z band, across the PanSTARRS array. The peak-to-peak fringing amplitude at this wavelength is 5%. (The individual gains of the detectors have not been normalized, and that accounts for the chip-dependent variations.)

6. POTENTIAL SOURCES OF SYSTEMATIC ERROR

We present below our current level of understanding of various sources of systematic error, steps taken to date, and what we perceive as the path forward. Table 3 summarizes our current estimate of the impact of systematic errors. The subsections following the Table provide the rationale for the entries. Since we have yet to measure and correct for stray and scattered light effects, specifically the difference between system sensitivity to diffuse light as opposed to resolved sources at the arcsec scale, our systematic error budget is currently dominated by our conservative estimate of the illumination correction, at the 5% level. If we succeed in achieving a factor of ten reduction in this systematic error (which as outlined below has been achieved by others) then we might hope to attain $\sim 0.2 - 0.5\%$ fractional uncertainty in instrumental throughput determination.

Table 3: Systematic Uncertainty Estimates for Night-time Throughput Calibrations.

Gremlin	Estimated σ_T/T
Photodiode Calibration Uncertainty	10^{-3} for 470 nm $< \lambda <$ 950 nm
	1.0 to 1.5 $\times 10^{-2}$ for $\lambda >$950 nm
	5.0 to 1.0 $\times 10^{-3}$ for 350 nm $< \lambda <$470 nm.
Ambient Light Fluctuations	$< 2 \times 10^{-3}$
Stray Light, "Illumination" Corrections[a]	5×10^{-2}
Wavelength Independent Screen Non-Uniformity	5×10^{-2}
Wavelength Dependent Screen Non-Uniformity[b]	2%
Spectral Purity	$< 5 \times 10^{-4}$ for $\lambda >$400 nm
Wavelength Calibration	10^{-2} on steep filter skirts
	$< 10^{-3}$ otherwise
Timing Latencies	$< 10^{-4}$
Camera Shutter Artifacts	$< 10^{-4}$
CCD or Photodiode Temperature	1% per degree C for $\lambda >$ 900nm

[a]This is our conservative estimate, with no corrections applied. Marshall & DePoy (2005) have demonstrated 6×10^{-3}.

[b] This applies to the r band, currently unconstrained at other wavelengths.

6.1. Uncertainty in the Photodiode Calibration

Our throughput measurement is only as good as the comparison standard we use. The combination of the QE curve of the photodiode, the photodiode's optical train, and the integrator circuit's capacitor comprise the metrology standard against which we are determining total system throughput. Fractional calibration uncertainty in the reference diode's QE curve is reported (NIST 2005; Larason *et al.* 1998) by NIST as 0.2% at 400 nm, 0.1% between 470 and 950 nm, rising to 1% for $\lambda > 950$nm.[3] This systematic uncertainty in QE dominates over other considerations such as the temperature coefficient of the integration capacitor times temperature changes over the duration of the measurement.

Even if dust flecks land on the calibration diode window in the time between the NIST calibration and our measurement, as long as this is a "grey" reduction in sensitivity it does not affect our relative throughput measurement. However monitoring the overall system throughput over extended periods of time will rely on both the optical configuration and diode sensitivity remaining constant.

6.2. Ambient Light Fluctuations

Our calibration technique relies upon our being able to determine the system's response to the light from the Ekspla NT242 OPO, and we do this by subtracting (from both the Gigapixel images and the photodiode signal) the flux seen in an equal amount of time. If the ambient background light comprises a fraction f of the *detected* flux in the imager, and this background varies by a fraction δ in the time between the illuminated and the background image, a 1% measurement of system sensitivity requires $f\delta < 0.01$. Particularly on the skirts of the filters, where f increases (since the instrument is detecting background light across the filter's entire optical passband, but sensitivity to the calibration light is suppressed), this strongly favors taking the calibration images on cloudy nights, when the ambient light level is both low and stable.

For the images taken at night, background light in the dome is essentially undetectable. A conservative estimate of the impact of ambient light fluctuations comes from the results shown in Table 2, which includes daylight measurements, at $\sigma_T/T < 2 \times 10^{-3}$.

[3]NIST's convention is to quote 2σ uncertainties ($k = 2$) and we have adjusted this to equivalent 1σ values, assuming Gaussian statistics.

6.3. Stray and Scattered Light Paths

Stray light is a potential problem when dome flats are used for sensitivity corrections, and our approach is not immune to this concern. Non-focused light paths can add flux to that from the direct, focused, path through the optical train. Only the wavelength-dependent variation in the stray light distribution will produce a systematic error in our throughput determination. Wavelength-dependent ghosting in the optics is one example of a scattered light path that might produce a variable gradient in illumination across the focal plane. This would then be misinterpreted as sensitivity variation, even if the system sensitivity is uniform. It is therefore important to obtain "illumination corrections" using point sources on the sky. We have not yet made this comparison for the PanSTARRS imager, but experience with other telescopes suggests that the illumination correction could be as large as 5%, and we will adopt this as our current estimate of the systematic error for stray and scattered light. We consider this to be a very conservative estimate, since only the wavelength-dependent portion of the illumination correction will afflict our determination of system throughput.

Marshall & DePoy (2005) have demonstrated using dome flats to achieve consistent photometric zeropoints at a level ten times better than our conservative estimate of systematic errors due to our not having made illumination corrections. Regnault *et al.* (2009) describe millimagnitude residual uncertainties after making careful illumination corrections, and in the future we hope to achieve similar performance, after measuring and making illumination corrections.

An illumination screen that only projects light over the range of angles seen by the camera ($\sim 3^o$ for PanSTARRS and LSST) would greatly reduce the stray light contribution. We have such a system currently under development (Gressler *et al.*, 2010).

6.4. Wavelength-Independent Illumination Screen Non-Uniformity

The camera pixels sense light primarily from a common area on the flatfield screen. We estimate that a 10% fractional uniformity in surface brightness should produce illumination on the focal plane that is uniform at the 1% level. We did not achieve this level of uniformity in the configuration used to obtain the data described here, so there is a potential grey multiplicative variation across the focal plane.

As long as the spatial surface brightness distribution of the screen does not exhibit a significant variation with wavelength, we can reliably use the data to assess the spectral sensitivity of each pixel, independently. Wavelength independent illumination variations impart a multiplicative grey variation in measured system response across the focal plane. This

then falls into the category of effects that will compensated for with an on-sky illumination correction, and the systematic error from wavelength-independent screen illumination is degenerate with other illumination correction effects, such as vignetting, etc. We therefore adopt the same systematic uncertainty here as that for stray and scattered light, 5×10^{-2}.

6.5. Wavelength-Dependent Illumination Screen Non-Uniformity

Comparing pixel response functions across the focal plane is undermined by any wavelength-dependent variations in focal plane illumination. Furthermore, if the pixels in the camera and the calibration photodiode intercept a wavelength-dependent difference in flux from the screen, a systematic error is introduced in the wavelength response of even a single pixel. Finally, even if the screen illumination is completely flat across all wavelengths, spectral variation in the reflections that feed stray and scattered light paths could introduce a systematic error in the measured response function.

A careful and thorough investigation of these different contributions will be a topic for future work, and for the purpose of this paper we will restrict our attention to the r band.

The data in Figures 7 and 8 indicate that away from the filter skirts, annular averages of r band system response (which eliminate first order gradients across the focal plane) are radius-independent to a few percent. Pending further analysis we will adopt the value of 2% as an estimate of the potential systematic error due to wavelength-dependent illumination effects, within the r band, but further investigation is needed.

6.6. Spectral Purity and Optical Bandwidth

The tunable Ekspla NT242 OPO produces light at numerous wavelengths (355, 512, 1064 nm) in the process of generating the photon pair from the downconversion in the OPO. Of particular concern would be leakage of one of these unwanted wavelengths in the passband being measured, or leakage light conspiring with (say) a red leak in an interference filter. We used the Ocean Optics spectrograph to verify that (with one exception) the light sent into the optical fiber had undetectably low ($< 5 \times 10^{-4}$) contamination light. The exception arises when wavelengths $\lambda < 400$ nm are requested, which the Ekspla NT242 OPO produces by frequency-doubling of OPO output light at 2λ. In this regime there is significant leakage light, which led us to avoid observations at the blue edge of the g band, pending the installation of a short-pass filter. While the g filter would likely sufficiently block the red leakage light from reaching the instrument, the calibration diode would see this light

from the screen, producing a systematic error in the reported flux. In a subsequent run will place a short-pass filter in the Ekspla NT242 OPO for scanning the region below 400 nm.

The optical bandwidth of the calibration light is another potential source of systematic error, since the measured response function is the actual monochromatic response convolved with the bandwidth of the calibration light. At the longest wavelengths we probed, $\lambda \sim 1\mu$m, the calibration light had a bandwidth of under 0.5 nm. This consideration is one of the main reasons we favor the use of the tunable laser over a monochromator, from which it is difficult to achieve the desired spectral power density.

6.7. Wavelength Calibration

An error in wavelength calibration will of course shift the measured curves accordingly. We showed above that our wavelengths are known to an uncertainty of $\sigma_\lambda \sim 0.2nm$. This effect is most pronounced on the steep edges of the interference passbands, and the error introduced in transmission is $\sigma_T = \sigma_\lambda dT/d\lambda = 0.2 \times 0.06 \sim 1\%$, since the steepest slope we see in the filter skirts is $dT/d\lambda = 0.06$ nm^{-1}. Away from the filter skirts the systematic error due to wavelength miscalibration is a factor of ten lower, under a part per thousand.

6.8. Timing Latencies and Shutter Artifacts

Although the PanSTARRS image headers do contain actual shutter open time with msec accuracy, our mode of operation is inherently insensitive to timing jitter. Our method of taking data assures that each pixel is exposed to the calibration light for exactly the same time period, regardless of shutter imperfections or asymmetries. As long as the fixed dose of laser light is provided during the interval we are certain the camera shutter is open, variation in shutter open times only influences our correction for ambient light levels, and at night this is negligible. We therefore assess the systematic error from shutter open timing to contribute less than 10^{-4} to our flux uncertainties, for night-time calibration data.

Another potential source of background light mis-correction comes from network latency in the client-server configuration we used. We will adopt an estimate of 5 msec for jitter in the timing between the computers, but again this only influences the ambient light correction, which for night-time calibration images is negligible anyway, and so we assign this a contribution of $< 10^{-4}$.

6.9. CCD and Photodiode Temperature Variations

The process of converting incident photons into photoelectrons is assisted by thermal excitation of electrons into the conduction band of Silicon. The Gigapixel camera's sensitivity is therefore a function of the focal plane temperature. This is most pronounced in the y band, especially since the red edge of the y band is defined by the falling CCD QE curve. Similarly, the sensitivity of the calibration photodiode to NIR light depends to some extent on its temperature.

As long as both of these dependencies are known, we can account for the temperature-dependence of the sensitivity of both the calibration diode and the focal plane array. We can measure the temperature of the calibration diode with sufficient accuracy to properly account for its QE(T,λ). The thermometry on the Gigapixel camera is somewhat more problematic, since the temperature sensors are some distance from the detectors. Our approach to this in the future will be to map out the system response function at a variety of camera temperature settings, and establish an empirical relationship between system throughput and the temperature data provided by the camera. We can then use an appropriate response function for each survey image, based on the temperatures reported in the image headers.

For the data presented here, we assess the systematic due to temperature-dependent QE effects to be under 10^{-3} for $\lambda < 900\ nm$, rising to $1\%/^o$C at 1 μm.

7. DISCUSSION

We have shown the ability to obtain a succession of monochromatic calibration images that exhibit short term repeatability at the level of a few parts per thousand. Our long term goal is to provide, for each survey image and associated photometric catalog, the effective passband through which the image was acquired. This would include both the instrumental response function at the location of the source, as well as the estimate of atmospheric transmission along the appropriate line of sight.

These results encourage us to further pursue this technique to both measure and monitor system sensitivity over the course of the PanSTARRS survey. We also intend to use the system described here to measure the dependence of the response function on CCD device temperature, in the phonon-assisted photoconversion regime at wavelengths near 1 μm. Another interesting measurement would be to compare the response function before and after mirror cleaning or dust deposition events.

We can also use these instrumental sensitivity data in conjunction with measurements of

atmospheric transmission to compare synthetic photometry with observations, as described in Stubbs & Tonry (2006), across different regions of the focal plane. Table 4 is an initial exploration of this approach. We took model atmospheres from Kurucz (1996) and converted them to photon spectral energy (PSED) distributions $\Phi_\gamma(\lambda)$. We then integrated[4] these photon distributions over the seven distinct annular r band response functions, to assess the photometric perturbation that would arise from the observed radial variation in the sensitivity functions. We computed for each radial annulus a the "raw" synthetic magnitude

$$m(a)_{raw} = \int T(a,\lambda)\Phi_\gamma(\lambda)d\lambda,$$

and also a normalized magnitude that corresponds to constructing a photon-flat

$$m(a)_{normalized} = \frac{\int T(a,\lambda)\Phi_\gamma(\lambda)d\lambda}{\int T(a,\lambda)d\lambda},$$

where a=1,2...7. The normalized magnitudes correct for the radial variation in the integrated area under the sensitivity curve.

Table 4 shows the resulting magnitude differences, $\Delta m = m_{edge} - m_{center}$, between the edge ($a$=7) and the center ($a$=1) of the PanSTARRS field, for different stellar types. The second column in Table 4 shows that the raw flux at the field edge ranges from 3.7% to 4.6% higher than the value at the center, with the variation being monotonic with decreasing stellar temperature. This is consistent with the sensitivity function behavior shown in Figure 8: stars at the edge appear brighter, and red stars more so than blue ones.

If we compare instead the "normalized" magnitudes (the third column in Table 4) the flux excess diminishes by a factor of 5 to 20, depending on stellar temperature. However, even after flux normalization at each radial annulus by $\int T(a,\lambda)d\lambda$, a scalar quantity that implicitly weights each wavelength equally, the third column in the Table still shows up to $\sim$1% perturbations in stellar photometry (*e.g.* $\Delta m_{normalized}$(O5V) - $\Delta m_{normalized}$(M6V)=0.0094) that depend on both stellar temperature and separation across the field.

We conclude from this synthetic photometry exercise that we can expect half-percent level r band zeropoint shifts between the center and the edge of the field, even after flat-fielding, for a given stellar type. Looking across stellar types (from O to M class stars) we can expect systematic zeropoint differences at the percent level, between the center and the edge of the field. As outlined in Stubbs & Tonry (2006), knowing the system throughput for each pixel and for each wavelength will allow us to account for these effects in detail.

[4]We have omitted the effect of atmospheric attenuation since our interest here is only to explore the effect of focal plane position-dependence of the sensitivity function.

Table 4: Influence of Observed r band Center-to-Edge Variations on Synthetic Stellar Photometry.

Stellar Type	Edge-Center Δm_{raw}	Edge-Center $\Delta m_{normalized}$
O5V	-0.0367	0.0068
O7V	-0.0368	0.0068
O9V	-0.0368	0.0067
B1V	-0.0371	0.0065
B3V	-0.0374	0.0061
B5V	-0.0376	0.0059
B8V	-0.0379	0.0056
A1V	-0.0385	0.0050
A3V	-0.0388	0.0047
A5V	-0.0393	0.0042
F0I	-0.0391	0.0044
F0V	-0.0391	0.0044
F2V	-0.0411	0.0025
F5V	-0.0417	0.0019
F8V	-0.0420	0.0015
G2V	-0.0425	0.0011
G5I	-0.0425	0.0011
G5V	-0.0426	0.0009
G8V	-0.0429	0.0007
K0V	-0.0434	0.0001
K4V	-0.0450	-0.0015
K7V	-0.0460	-0.0025
M2V	-0.0457	-0.0021
M4V	-0.0461	-0.0026
M6V	-0.0461	-0.0026

This suggests that pushing the photometric precision beyond the 1% level will likely require a more sophisticated flat-fielding approach, that takes full advantage of the system's measured spectral response function (as well as a determination of atmospheric transmission). Also, the determination of "illumination corrections", by rastering a source around the focal plane and requiring consistent results, will be PSED-dependent at the percent level.

We are now in a position to quantitatively assess various flat-fielding schemes, such as performing a joint analysis of photometric data from all bands, that take into account the position-dependence (and also, if needed, time-dependence) of the system's response function.

Finally we note that a full-aperture calibration taken of a distant source of known radiance, even at just one wavelength, would suffice to determine the single overall multiplicative term we need to extend these measurements to an absolute calibration of the PanSTARRS system. This would require appropriate knowledge and correction for atmospheric transmission, but the single wavelength could be judiciously chosen (such as $\lambda \sim 808$ nm, also convenient for laser diode sources) to coincide with good detector QE as well as high and stable atmospheric transmission.

Facilities: PanSTARRS

We are grateful to the National Institute for Standard and Technology (under award 70NANB8H8007), the LSST Corporation, Harvard University and the Department of Energy Office of Science (under grant DE-FG02-91ER40654) for their support of this work. The dedication and competence of the scientific and technical staff of PanSTARRS project were essential to the success we report here. In particular we are grateful to Will Burgett, Robert Calder, Ken Chambers, Greg Gates, Tom Melsheimer, Jeffrey Morgan, and Shannon Waters for their invaluable assistance. Conversations with Tim Axelrod, David Burke, Darren DePoy, Ned Henry, David Hogg, Paul Horowitz, Zeljko Ivezic, Eli Margalith, John McGraw, Armin Rest, Abi Saha, Nick Suntzeff, Chris Smith, Will High and Pete Zimmer were very valuable in designing and refining the technique described here. We are also grateful to the anonymous hitchhikers in the Haleakala National Park who provided us with the opportunity to accumulate the good karma needed for this endeavor.

REFERENCES

Adelman, S. J., Gulliver, A. F., Smalley, B., Pazder, J. S., Younger, P. F., Boyd, L. J., Epand, D., & Younger, T. 2007, The Future of Photometric, Spectrophotometric and

Polarimetric Standardization, ASP Conference Proceedings **364**, 255.

Albert, J., Foster, K., Battat, J., Dupuis, G., Fransham, K., Koopmans, K., & Jarrett, M. 2009, arXiv:0908.3343.

Barr Associates, 2008 private communication.

Pierre Auger Collaboration 2010 Astroparticle Physics **33**, 108.

Bohlin, R. C. 2007, in The Future of Photometric, Spectrophotometric and Polarimetric Standardization, Sterken, ed., ASP Conference Proceedings **364**, 315.

Brack, J.T *et al.* 2004 Astroparticle Physics **20**, 653.

Burke, D. *et al.*, 2010 in preparation.

Doi, M. *et al.*, 2010 arXiv:1002.3701, AJ in press.

Eppeldauer, G. P., Yoon, H. W., Zong, Y., Larason, T. C., Smith, A., & Racz, M. 2009, Metrologia, **46**, 139

Gressler, W. *et al.* 2010 Proc. SPIE, in press.

Hayes, D. S., & Latham, D. W. 1975, ApJ, **197**, 593.

High, F. W., Stubbs, C. W., Rest, A., Stalder, B., & Challis, P. 2009, AJ, **138**, 110

Holberg, J. B. and Bergeron, Pierre, ApJ 2006 **132**, 1221.

Kaiser, M. E., Kruk, J. W., McCandliss, S. R., Sahnow, D. J., Dixon, W. V., Bohlin, R. C., & Deustua, S. E. 2007, in The Future of Photometric, Spectrophotometric and Polarimetric Standardization, Sterken, ed. ASP Conference Proceedings **364**, 361

Kent, S., *et al.* 2009, Submitted to The Astronomy and Astrophysics Decadal Survey, arXiv:0903.2799v1.

Kurucz, R. L. 1996, M.A.S.S., Model Atmospheres and Spectrum Synthesis, **108**, 2

Larason, T., Bruce, S. , and Parr, A. 1998 NIST Special Publication 250-41.

Linder, E. V. 2009, Phys. Rev. D, **79**, 023509

Marshall, J.L. & DePoy, D.L. 2005 arXiv:astro-ph 0510233.

Megessier, C. 1995, A&A, **296**, 771.

NIST, 2005 calibration data provided for serial number I220 photodiode, private communication.

Onaka, P., Tonry, J. L., Isani, S., Lee, A., Uyeshiro, R., Rae, C., Robertson, L., & Ching, G. 2008, Proc. SPIE, **7014**, 12.

Perryman, M. A. C., *et al.* 2001, A&A, 369, 339

Regnault, N. et al. 2009 A&A, **506**, 999

Sterken, C., ed. 2007, The Future of Photometric, Spectrophotometric and Polarimetric Standardization, ASP Conference Proceedings **364**.

Stubbs, Christopher W. and Tonry, John L. 2006 ApJ, **646**, 1436.

Stubbs, C. W., *et al.* 2007, PASP, **119**, 1163.

Stubbs, C. W., *et al.* 2007, in The Future of Photometric, Spectrophotometric and Polarimetric Standardization, Sterken, ed. ASP Conference Proceedings **364**, 373.

Stuik, R. and Bijerkek, F. 2002 NIMA **489**, 370.

Tonry, J. L., Burke, B. E., Isani, S., Onaka, P. M., & Cooper, M. J. 2008, Proc. SPIE, **7021**, 9.

Vest, R.E. and Grantham, S. 2003 Applied Optics **42** 5054.